Numerical simulation of rim seal flows in axial turbines

J. Boudet, V. N. D. Autef, J. W. Chew, and N. J. Hills
University of Surrey,
Thermo Fluid Systems,
Guildford, UK

O. Gentilhomme
University of Sussex,
Thermo Fluid Mechanics Research Centre,
Brighton,UK

ABSTRACT

In a gas turbine, ingestion of hot gas into the high-pressure turbine disc cavities could cause metal overheat. To prevent this, cool air is taken from the compressor and ejected through the cavities. However, this sealing flow also reduces the overall efficiency, and a compromise has to be found between the level of ingestion tolerated and the losses. Recent advances made in applying Computational Fluid Dynamics to such configurations are presented, with the aim of better understanding the physical phenomena and providing reliable design tools. First, results showing the pumping effect of the rotating disc are presented, including the influence of flow instabilities observed in both computational and experimental results. Second, the influence of the main annulus pressure asymmetries are analysed on a simplified representation of an available experiment, showing the combined influence of asymmetries generated by vanes and struts. Finally, a rim seal geometry representative of aero-engine design is studied in comparison to experiment, exhibiting the coupled influence of the cavity instabilities and annulus asymmetries.

NOMENCLATURE

A	swirl flow angle to the axial direction
A_{gap}	rim seal gap area
C	tracer gas concentration ($C \in [0;1]$)
C_∞, C_{cool}	ambient and coolant air concentrations of tracer gas
C_D	rim seal discharge coefficient (model of Scanlon *et al*[9])
C_P	pressure coefficient
$C_w = m_{cool}/r_{hub}\mu$	non-dimensional coolant mass-flow
$C_{w,min}$	minimum value of C_w necessary to seal the cavity
$G_c = S_c/r_{hub}$	seal clearance ratio
f_{bld}	blade passing frequency
k	turbulent kinetic energy
k_{seal}	constant, function of the rim seal design (model of Chew[8])
m_{cool}	coolant mass flow
m_{in}, m_{out}	inward and outward mass flows through the rim seal
$\mathbf{n}$	local unity vector normal to surface S
N	number of guide vanes or struts
P	static pressure
P_{mean}	mean pressure for a given distribution
P_{cav}	characteristic pressure inside the cavity
P_{min}, P_{max}	minimum and maximum pressures inside the main annulus
P_i	main annulus inlet static pressure
P_{0i}	main annulus inlet stagnation pressure
r, θ, x	cylindrical co-ordinates
r_{hub}	main annulus hub radius
R	gas constant
$Re_x = \rho V_x r_{hub}/\mu$	main annulus axial Reynolds number
$Re_\theta = \rho\Omega r_{hub}^2/\mu$	rotational Reynolds number
S	artificial cutting surface through the rim seal
S_c	axial seal clearance
T	static temperature
v_i	flow velocity in the direction i ($i = x, y, z, r$ or θ)
$\mathbf{v}$	velocity vector
V_{dm}	mixed out radial velocity (model of Chew[8])
V_m	coolant mass flow-based velocity
V_x	mass flow-based velocity in the main annulus
x, y, z	cartesian co-ordinates
x_{stator}, x_{rotor}	stator disc and rotor disc main faces x-co-ordinate
y^+	distance to the wall in wall units

Paper No. 2915 Received on 20 September 2004, revised copy received on 2 May 2005, accepted 2 June 2005.
This paper was first presented at the RAeS Aerospace Aerodynamics Research Conference, September 2004.

Greek symbols

ε	turbulent dissipation
ϕ	sealing effectiveness
κ	non-dimensional cavity pressure $\kappa = (P_{cav} - P_{min})/(P_{max} - P_{min})$
μ	dynamic viscosity
ρ	density
Ω	rotational velocity
ψ	mass flow ratio through the rim seal (estimate of ϕ)

Symbols

$\bar{q}$	time average value of fluctuating quantity q
Δq	amplitude of fluctuating quantity q

Abbreviations

CFD	computational fluid dynamics
NGVs	nozzle guide vanes
OC	operating condition
RANS	Reynolds averaged Navier-Stokes
2D/3D	two/three-dimensional

1.0 INTRODUCTION

The improvement of turbomachinery efficiency over the past decades has been accompanied by an increase of the temperature at the outlet of the combustion chamber. Pressure to further improve efficiency and component life ensures continuing interest in thermal behaviour and cooling of turbine components. The present paper is concerned with the metal overheat that can result from the ingestion of the main annulus gas into the disc cavities located between consecutive stationary and rotating turbine blade rows. A common way to counter this effect is to take cool air from the compressor and eject it through the cavities into the turbine main annulus. However, this coolant flow is lost from the thermodynamic cycle and may also cause spoiling losses as it re-enters in the main gas path. Consequently, the coolant mass-flow has to be limited, finding a compromise between the level of ingestion tolerated and the loss of efficiency.

A first insight into the complex flow field generated between the cavity and the main annulus can be obtained by referring to different complementary studies. First, the flow inside the cavity is influenced by the rotor disc located on one side. As formulated by Von Kármán[1], a disc that rotates in a fluid medium imposes its rotation to the surrounding fluid and the resulting centrifugal force conveys the flow outward. This is called the *pumping effect*. Later, Batchelor[2] extended the study to a rotor-stator system. In this case, a rotating disc and a static disc are positioned face to face, delineating a cavity similar to that in a turbine. The pumping effect remains on the rotor, and fluid is driven inward on the stator face to feed the rotor boundary layer. Transition to turbulence is controlled by the rotational Reynolds number Re_θ and is governed by two types of instabilities (referred as Type I and Type II). However, instabilities are likely to occur even in the turbulent regime, as reported for example by Serre *et al*[3] at $Re_\theta = 3 \times 10^5$. If the gap is wide enough and the cavity shrouded to prevent ingestion, a rotating core is generated between the two disc boundary layers. The core velocity is about $0{\cdot}30\Omega$ if the flow is laminar, and $0{\cdot}43\Omega$ if turbulent.

A further feature of turbines is the injection of cool fluid through holes at the inner part of the cavity. This feeds the rotor boundary layer, and reduces the flow driven from the periphery by the stator. Owen and Rogers[4] studied the reduction of the core velocity and associated radial pressure gradient, as the level of feeding mass-flow is increased.

The flow field between the cavity and the main passage is also influenced by the pressure asymmetries inside the main annulus (i.e. non-axisymmetries), which drive the gas from the high-pressure zones to the lower ones. Phadke and Owen[5] discussed this effect and defined two different regimes:

- a rotation-dominated regime at small values of Re_x/Re_θ;
- an external flow-dominated regime at large values of Re_x/Re_θ, where the ingestion becomes independent of Re_θ and proportional to Re_x

In the experiment of Phadke and Owen, the transition to the second regime is related to the growing influence of the inherent circumferential pressure asymmetries. In a gas turbine, pressure asymmetries are various, coming for example from the combustion chamber or the preceding blade rows.

Finally, the geometry of the rim seal at the outer part of the cavity has a strong influence, providing the turbomachinery designer with the possibility of reducing the hot gas ingestion and consequently the necessary amount of cooling air. Phadke and Owen[6] studied the performance of seven different rim seal geometries without external flow. The most efficient geometries are those having a stator rim overlapping the rotor disc at the outlet of the cavity, which creates flow conditions countering ingestion. Also, the division of the cavity into different sections, separated by inner seals, helps protect the inner sections from hot gases by damping the pressure asymmetries. These design features are common in gas turbines, but published studies are mainly concerned with basic axial rim seals and single sectioned cavities.

From the empirical database, some predictive models have been developed to evaluate the level of ingestion inside the cavity. For the rotationally dominated regime, Bayley and Owen[7] worked on an experimental rig incorporating a stationary shroud with a simple axial seal. They obtained the following correlation for the minimum value of the coolant flow rate parameter $C_{w,min}$ required to prevent ingestion:

$$C_{w,\min} = 0{\cdot}61 G_c \, \mathrm{Re}_\theta \qquad \ldots (1)$$

Later, Chew[8] combined the momentum integral equations for cavity flows with a simple seal model, and obtained:

$$C_{w,\min} = 2\pi k_{seal} G_c \mathrm{Re}_\theta \left(V_{dm} \Big/ \Omega r_{hub} \right) \qquad \ldots (2)$$

where k_{seal} is an empirical constant function of the rim seal design and V_{dm} a mixed out radial velocity for the near wall flow at the outer radius of the cavity.

For the external flow-dominated regime, predictive methods have been developed using an orifice model. Recently, Scanlon *et al*.[9] proposed the following formulation for the outward and inward mass-flows (cf. Appendix for a description of m_{in} and m_{out}):

$$m_{out} = C_D A_{gap} \sqrt{\frac{2P_{cav}(P_{max} - P_{min})}{RT}} \left[\frac{\kappa\pi}{4} \right] \qquad \ldots (3)$$

$$m_{in} = C_D A_{gap} \sqrt{\frac{2P_{cav}(P_{max} - P_{min})}{RT}} \left[\frac{1}{2} \left(\sqrt{1-\kappa} - \kappa \, \mathrm{ArcCosh}\left(1/\sqrt{\kappa} \right) \right) \right]$$

where C_D is the discharge coefficient of the rim seal, A_{gap} the gap area, P_{cav} is a characteristic pressure inside the cavity, $[P_{min}; P_{max}]$ is the outer annulus pressure variation range, and $k = (P_{cav} - P_{min})/(P_{max} - P_{min})$.

https://doi.org/10.1017/S000192400070042X Published online by Cambridge University Press

The design improvement of gas turbines now requires the representation of the complex unsteady flow physics. The present paper focuses on the study of such effects, and their simulation by CFD. Computations are presented in comparison to available experimental data in order to assess the numerical capacities and requirements. In particular, comparisons are made with measurements of two parameters:

(*i*) The sealing effectiveness.
On an experimental rig, tracer gas may be supplied at the coolant inlet with a concentration C_{cool}. If the main annulus inlet concentration is C_∞, then the sealing effectiveness at a given point inside the cavity is defined by:

$$\phi = \frac{C - C_\infty}{C_{cool} - C_\infty} \quad \ldots (4)$$

where C is the tracer gas concentration at this point. The lower the value of ϕ, the stronger is ingestion of main annulus flow down to this point inside the cavity.

In computations, tracer gas may be represented by a passive scalar, and ϕ is calculated as above. Where the passive scalar option is not available, the mass flow ratio through the rim seal (ψ) is used below to indicate the degree of ingestion, as described in the Appendix. In simple models, other workers sometimes assume that ϕ and ψ are equal, but this is not necessarily true.

(*ii*) The pressure coefficient inside the cavity.
The ingestion of main annulus flow tends to modify the level of swirl inside the cavity, which has a direct influence on the radial pressure gradient. For example, if the main annulus flow is characterized by a higher swirl than the cavity flow, ingestion increases the swirl inside the cavity and makes the radial pressure gradient steeper. This is generally the case when the rim seal is located downstream of turbine guide vanes.

The study of the unsteady aspects and their representation by CFD will be carried out on three different rigs (A, B, and C), at different operating conditions. In Section 2, the pumping effect is addressed on simplified geometries (rig A at low cross flow, and rig B), with particular attention to the occurrence of instabilities. In Section 3, the influence of the main passage pressure asymmetries is considered on rig A at high cross flow, varying the amplitude and the periodicity of the perturbation to represent different origins (stator vanes, struts). In Section 4, a geometry representative of a gas-turbine is studied (rig C), which combines the preceding effects. Finally, conclusions are drawn in Section 5.

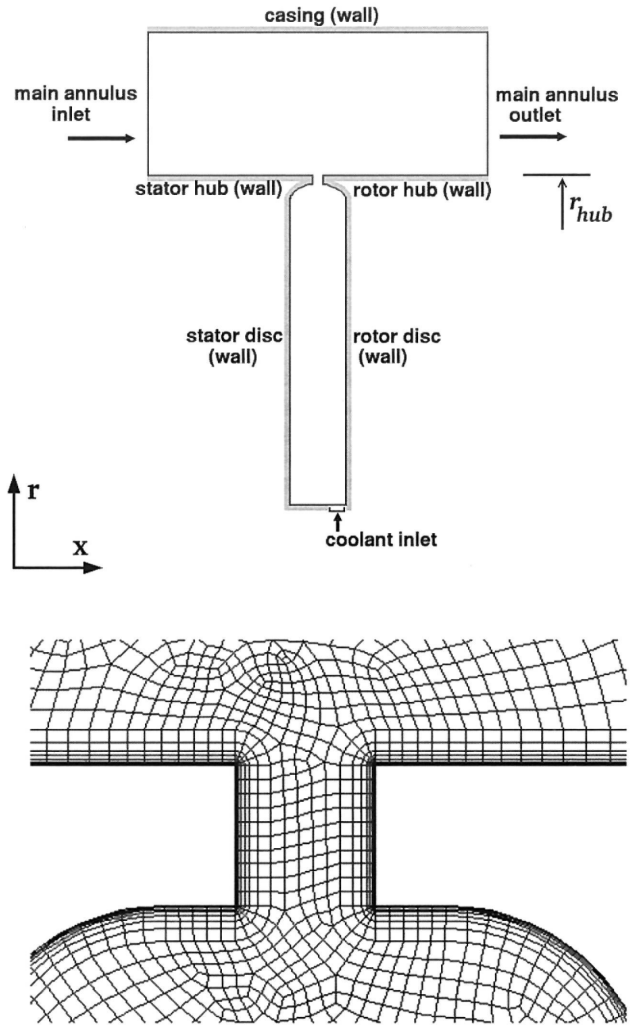

Figure 1. [rig A] Lateral view of the axisymmetric computational domain, and, (bottom) close-up view of the mesh around the rim seal. The main annulus height is 0·0252m, and the domain extends over 0·060m in the axial direction. The cavity height is 0·058m (between the bottom and the main annulus hub radius), and the axial width is 0·01m. The rim seal clearance is 0·002m.

2.0 DISC PUMPING EFFECTS

2.1 Rig A (low cross flow)

This section presents a numerical study on the pumping effect. The configuration chosen partly represents a turbine facility studied at the University of Sussex by Gentilhomme *et al.*[10, 11], based on the Gnome H1200 Power Turbine Module (helicopter engine). For this study, the rotor speed is Ω = 1,000rad/s and the rotational Reynolds number $Re_\theta = 1{\cdot}6 \times 10^6$. Because only the pumping effect is addressed, the computed geometry is simplified: the model does not include Nozzle Guide Vanes (NGVs) or blades. As shown in Fig. 1, the computational domain consists of a short main annulus and a cavity, with an axial rim seal.

The computations are carried out using FLUENT[12], a commercial CFD code solving the RANS equations. The 2D grid includes 5,800 grid points, refined in the near-wall region (cf. Fig. 1). It is extended in the circumferential direction to obtain the 3D grid over a 90 deg sector, with around 10^6 grid points. The turbulence is modelled using a k-ε model with enhanced wall treatment. In the near wall region, if the mesh is fine enough ($y+ \leq 5$), the viscous sublayer is resolved directly by the one-equation model of Wolfstein[13]. Otherwise, standard wall functions[12] are used.

A purely axial velocity is specified at the inlet of the annulus (V_x = 10ms^{-1}), and the exit is considered as a simple *'outflow'*, assuming a zero normal gradient for all flow variables except pressure. The coolant air enters through the bottom right of the cavity via a fixed *'mass flow inlet'* condition. No-slip condition on walls and periodic conditions (in the 3D simulations) are used to complete the boundary settings. Steady 2D axi-symmetric, and then 3D unsteady calculations assuming circumferential periodicity on a 90deg sector, are carried out for a range of coolant mass flows. Convergence of the solution is checked through satisfying residuals, overall mass balance (error: $\leq 10^{-1}$% of the inlet mass flow), and overall angular momentum balance (error lower to 1% of representative wall moments for 2D computations, and up to 15% in 3D computations).

The present computations consider a very low cross-flow passing through the annulus. Although this particular configuration is not

https://doi.org/10.1017/S000192400070042X Published online by Cambridge University Press

included in Gentilhomme's experiments, the empirical correlation of Bayley and Owen[7] (cf. introduction, Equation (1)) can be used. In absence of external flow, Chew[8] established a formula linking the sealing effectiveness ϕ to C_w that is in good agreement with experimental data for high values of r/r_{hub}:

$$\phi = \frac{C_w}{0{\cdot}8\,C_w + 0{\cdot}2\,C_{w,min}} \quad \ldots (5)$$

where $C_{w,min}$ represents the minimum amount of coolant flow necessary to seal the cavity. This correlation is compared to the computational estimate of ϕ calculated using a passive scalar feeding at the coolant inlet ($C_{cool} = 0{\cdot}01$).

Figure 2 shows the sealing effectiveness ϕ at $r/r_{hub} = 0{\cdot}95$ on the stator disc, against the non-dimensional coolant mass flow C_w. First, the 2D computations underestimate ingestion (i.e. higher value of ϕ). But 3D computations are close to the correlation even though the geometry and boundary conditions are axi-symmetric. This leads to consideration of possible natural asymmetries generated by the flow. This is investigated by Fig. 3, which shows the instantaneous concentration of tracer gas on the surface defined by $r = r_{hub}$, for the 3D solution. Lobes are observed above the rim seal: high concentration zones correspond to ejection of coolant gas ($C_{cool} = 0{\cdot}01$), and low concentration zones correspond to ingestion of main annulus gas ($C_\infty = 0$). The flow exhibits 56 lobes for the whole circumference, which rotate at about 3% of the disc speed in the stationary frame of reference. This is calculated by monitoring the unsteady pressure at several positions on the seal and its surroundings. The oscillations of highest amplitude are obtained inside the seal.

Increasing the annulus mass flow results in a higher influence of the annulus flow and the suppression of the instability. This is the configuration studied in Section 3, which addresses the regime dominated by annulus pressure asymmetries.

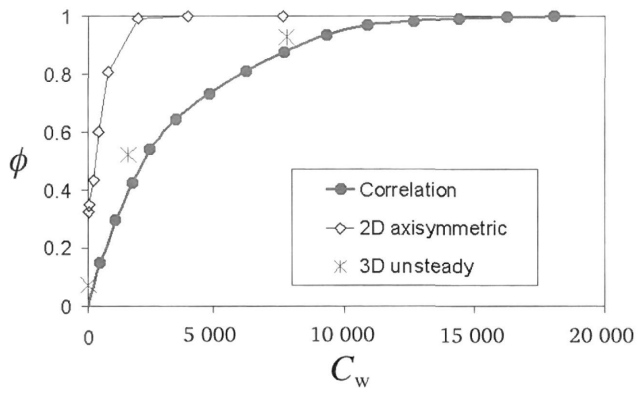

Figure 2. [rig A] Sealing effectiveness ϕ at $r/r_{hub} = 0{\cdot}95$ against the non-dimensional coolant mass flow C_w, for a low annulus mass flow: $V_x = 10\text{ms}^{-1}$. No asymmetry is enforced in the computations.

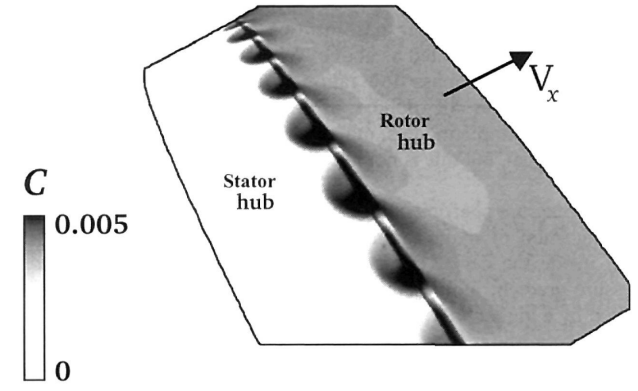

Figure 3. [rig A] Computed tracer gas concentration on the annulus hub at $C_w = 1{,}520$, for a low annulus mass flow ($V_x = 10\text{ms}^{-1}$). The main annulus hub (stator hub + rotor hub) is shown in perspective from the top, and the arrow represents the main flow direction in the annulus. The grid covers 90deg in the circumferential direction, and no asymmetry is enforced.

2.2 Rig B

Circumferential patterns have also been computed and confirmed experimentally by Cao *et al*[14] on another rig, at industrial operating conditions (strong main annulus mass flow). The geometry considered by these workers (here named rig B) is shown in Fig. 4. It is a simplified representation of the 2nd stage disc cavity of a two-stage axial turbine rig operated by Alstom Power. This seal geometry is more typical of a steam turbine than a gas turbine, but is of interest for the similar unsteady effects observed to those at rig A and for the direct experimental verification.

The operating condition for this study corresponds to $\text{Re}_\theta = 6 \times 10^6$. The main annulus inlet Mach number is 0·56 and the swirl angle $A = 78$deg. Coolant flow level is characterised by $C_w = 5{,}867$, corresponding to $V_m/V_x = 0{\cdot}06$ for the 2mm gap, and $V_m/V_x = 0{\cdot}03$ for the 4mm gap. In the external flow dominated regime referred to in the introduction, the parameter V_m/V_x is the most representative of coolant flow rate (for example, the experimental data obtained by Gentilhomme *et al*[10, 11] tend to merge when plotted against V_m/V_x). The FLUENT[12] CFD solver is used again, solving unsteady incompressible RANS equations with the standard k-ε turbulence model (+ wall functions) and the SIMPLE pressure correction algorithm. The spatial discretization uses a 2nd order upwind scheme, and the time step corresponds to 0·0064 of a disc revolution (implicit, second order temporal scheme). Concerning the boundary conditions, total pressure and tangential velocity are imposed at the annulus inlet, extracted from a throughflow calculation for the turbine. Static pressure is imposed at the outlet, with a radial equilibrium condition. A mass flow condition applies at the coolant inlet and no-slip conditions on the walls.

A lateral view of the computational domain is presented in Fig. 4. The mesh is swept in the circumferential direction to create axi-symmetric 90deg and 360deg sector grids ($0{\cdot}66 \times 10^6$ and $2{\cdot}45 \times 10^6$ points respectively). Balance holes are represented in the rotor face in some non-axi-symmetric grids, but the net sealing mass flow through the rim seal is kept equal to the cases without balance holes.

Figure 5 shows the pressure coefficient inside the cavity:

$$C_p = \frac{P - P_{(r/r_{hub}=1)}}{P_{0i} - P_i} \quad \ldots (6)$$

where $P_{(r/r_{hub}=1)}$ is the static pressure in the seal, and P_{0i} and P_i are the total and static pressure at the main annulus inlet ($P_{0i} - P_i$ is the dynamic head). For the 2mm axial clearance calculations, the experimental and computational results are close to the solution for a forced vortex rotating at $0{\cdot}5\Omega$. This is consistent with the classic sealed rotor-stator case for which a core rotating at about $0{\cdot}43\Omega$. is expected. For the 4mm clearance, the slope is steeper, corresponding in the outer part of the cavity to the solution of a forced vortex rotating at Ω. This must be due to the ingestion of high swirl flow from the main annulus. The best CFD results for the larger gap are obtained using the 360deg sector grid with balance holes, but all the computations are in reasonable agreement with the measurements. This is despite the neglect of the stationary and rotating blades in the CFD models.

Figure 6 shows instantaneous radial velocity and pressure contours, on an x-plane at 0·529mm before the rotor disc, for the 4mm

https://doi.org/10.1017/S000192400070042X Published online by Cambridge University Press

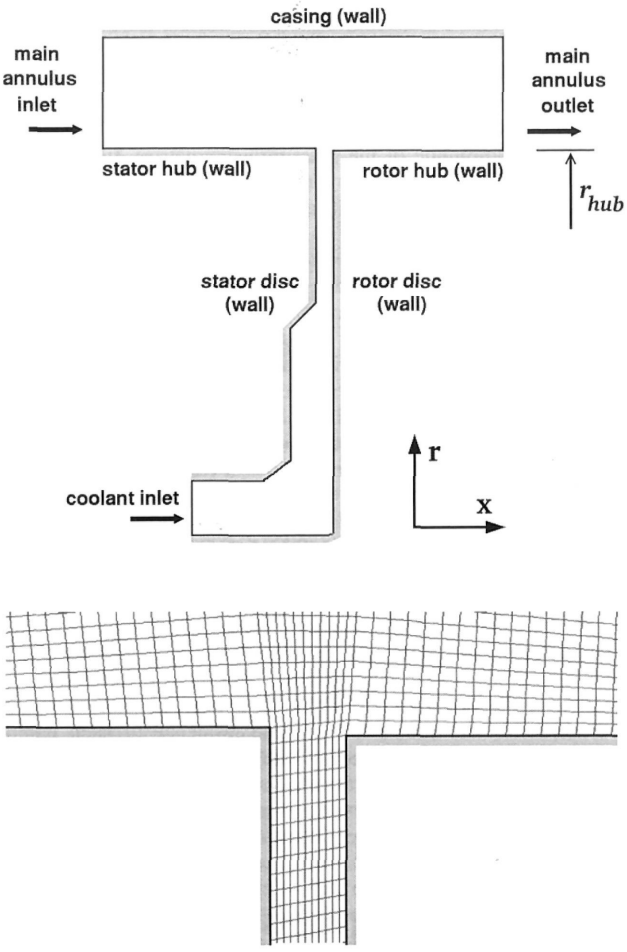

Figure 4. [rig B] Lateral view of the computational domain, and (bottom) close-up view of the mesh around the rim seal. The main annulus height is 0·033m, and the domain extends over 0·120m in the axial direction. The cavity height is 0·115m (between the bottom and the main annulus hub radius), and two rim seal widths have been tested: 0·002m and 0·004m (here the latter is represented).

gap, 360deg axisymmetric grid CFD solution. It appears that the steady axi-symmetric flow that would be obtained in a 2D computation is unstable. A lobed flow pattern develops around the circumference, rotating at a slightly lower velocity than the rotor disc. The 90deg grid case also gives a lobed flow pattern with a similar length scale, but the structure is modified by the periodic condition. With the smaller gap of 2mm, the length scale and the amplitude of these lobes are reduced. Note that, as for rig A, these rotating flow patterns occur despite the geometry and boundary conditions being axi-symmetric. Experiments carried out later with fast response pressure transducers confirm those numerical results, presenting fluctuations with an amplitude $\Delta P \approx 2{,}500$Pa, and a frequency of about 700Hz, as in the computations. Further details are given by Cao *et al*[14].

3.0 ANNULUS PRESSURE ASYMMETRY EFFECTS (RIG A, HIGH CROSS FLOW)

The results presented in this section correspond again to rig A. The numerical configuration is the same, but the annulus flow is increased to $V_x = 100\text{ms}^{-1}$, and an inlet swirl angle $A = 70$deg is imposed (except for the first 2D computation). The operating condi-

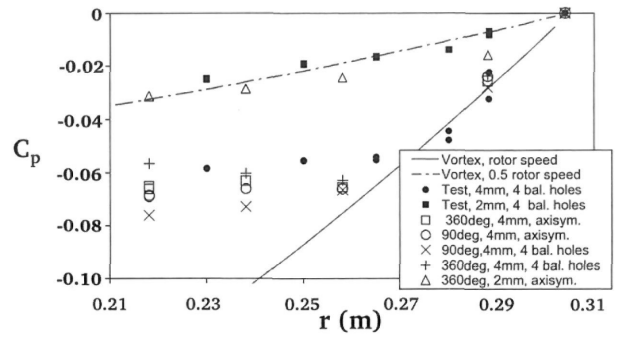

Figure 5. [rig B] Pressure coefficient on the cavity stator disc.

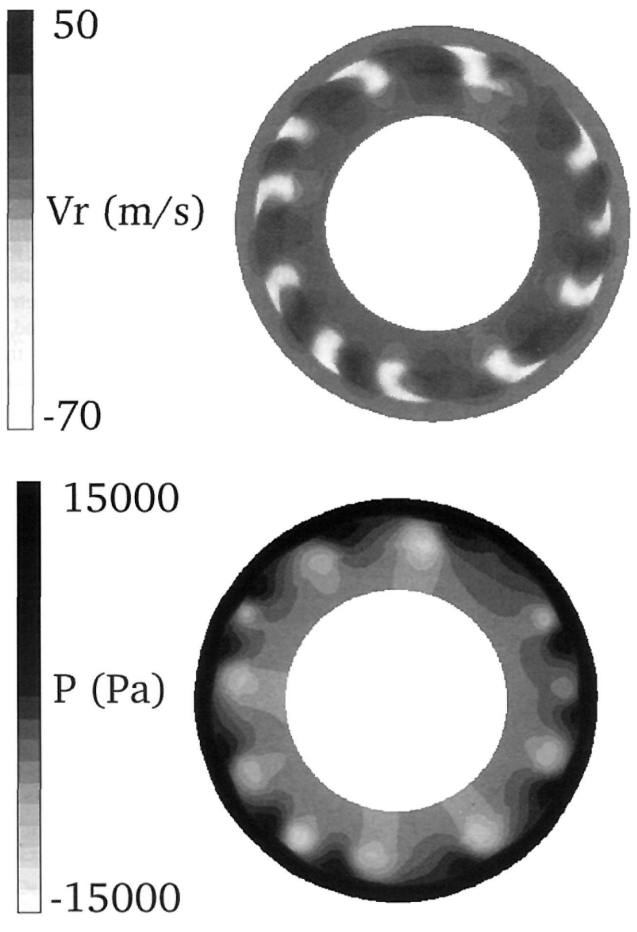

Figure 6. [rig B] Instantaneous radial velocity, and pressure, for the 4mm gap, 360deg axisymmetric grid, on an *x*-plane located 0·529mm before the rotor disc. No asymmetry is enforced in the computation.

tion of the computations ($Re_\theta = 1{\cdot}6 \times 10^6$) lies between two experimental operating conditions ($Re_\theta = 9{\cdot}04 \times 10^5$ for OC2 and $Re_\theta = 2{\cdot}83 \times 10^6$ for OC1). Again, the computations are carried out with FLUENT[12]. The residuals are checked for convergence, the mass balance error is $\leq 10^{-5}$% of the inlet mass flow, and the angular momentum balance error is negligible compared to the momentum fluxes in the main annulus.

In Fig. 7, the sealing effectiveness ϕ at $r/r_{hub} = 0{\cdot}95$ on the stator disc is plotted against the ratio V_m/V_x, for different computations

https://doi.org/10.1017/S000192400070042X Published online by Cambridge University Press

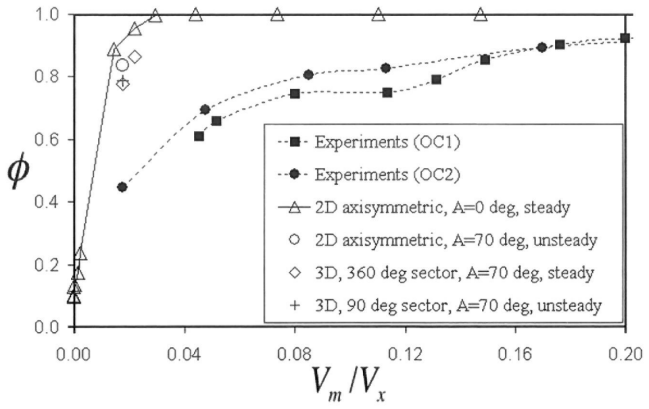

Figure 7. [rig A] Sealing effectiveness at r/r_{hub} = 0·95, for a high annulus mass flow (V_x = 100ms^{-1}). Computations use axisymmetric grid and boundary conditions, and 'A' represents the swirl flow angle at the annulus inlet (A = 70deg in the experiment).

using axi-symmetric boundary conditions. The first two curves in the figure legend present the experimental data for the two operating conditions, and show that quite good agreement is obtained when plotting against V_m/V_x. The next curve corresponds to a 2D axi-symmetric steady simulation with no swirl at the annulus inlet (v_θ = 0ms^{-1}), which greatly underestimates the ingestion. For the next simulations, a swirl angle of 70 deg (v_θ = 275ms^{-1}) is introduced in the annulus, representing the deflection by the NGVs. The introduction of the swirl velocity is respectively tested on a 2D axi-symmetric unsteady simulation, a 3D steady simulation (360deg sector) and a 3D unsteady simulation (90deg sector). The improvement of the solution compared to the experimental measurement is relatively small. Contrary to the weak cross-flow configuration (Subsection 2.1), the flow appears axi-symmetric, and shows no unsteadiness. It seems that in this case, when the external flow reaches a sufficient speed, it dominates and suppresses the instability.

Next, the study focuses on the possible influence of the circumferential pressure asymmetries, such as those generated by the NGVs upstream of the seal. An approximate potential flow solution is used to modify the annulus inlet conditions as previously employed by Chew *et al*[15]. This assumes a small perturbation about a base flow and may be written as follows:

$$
\begin{aligned}
P &= \overline{P} + \Delta P \,\mathrm{Cos}(N\theta)\, e^{-\frac{xN}{r}} \\
v_x &= \overline{v}_x - \frac{\Delta P}{\rho\sqrt{\overline{v}_\theta^2 + \overline{v}_x^2}}\,\mathrm{Cos}(N\theta + A)\, e^{-\frac{xN}{r}} \\
v_r &= 0 \\
v_\theta &= \overline{v}_\theta - \frac{\Delta P}{\rho\sqrt{\overline{v}_\theta^2 + \overline{v}_x^2}}\,\mathrm{Sin}(N\theta + A)\, e^{-\frac{xN}{r}}
\end{aligned}
\qquad \ldots (7)
$$

where (v_x, v_r, v_θ) are the velocity components written in the cylindrical co-ordinate system. The unperturbed flow field is given by $(\overline{v}_x, 0, \overline{v}_\theta)$ and $\overline{P}$, and A is the mean annulus swirl angle to the axial direction. The perturbation is determined by N, the number of guide vanes and ΔP, the magnitude of the pressure perturbation (at x = 0).

The velocity asymmetries are imposed in FLUENT[12] at the inlet of the annulus, with N = 26 (number of guide vanes). The value of ΔP is adjusted to obtain an amplitude of pressure fluctuations around 20% of the dynamic head (i.e. 5,000Pa) at 4·5mm upstream of the rim seal. This matches the pressure measurements taken at this location. The domain is slightly shortened in the axial direction (x) from that described above, to reduce the pressure variation required at the inlet plane. In the circumferential direction, three NGV pitches are represented, over 41·5deg. Figure 8 shows the sealing effectiveness at V_m/V_x = 0·038, for the experiment (1st curve), for a computation without pressure asymmetry (2nd symbol) and for a computation with pressure asymmetries (3rd symbol). The imposed pressure asymmetry leads to more ingestion, but still leaves a significant discrepancy with the measurements. Further tests show the ingestion is quite sensitive to the amplitude of the pressure asymmetries. Increasing the amplitude of the fluctuations by a factor 1·2 (4th symbol) leads to a sealing effectiveness of 0·79 instead of 0·88 (experimental data interpolate around 0·62).

The underestimation of ingestion could be due to larger scale circumferential pressure asymmetries, caused by the four struts further upstream or by an inlet distortion in the rig. As indicated in Equation (7), axial decay is slower for larger scale asymmetries and there could be some impact in the rim seal region. However, there is no experimental data for these asymmetries, so this is somewhat speculative and exploratory. Extending the CFD model to cover a 90deg sector allows imposition of both a perturbation with N = 28 (representing the NGVs) and another with N = 4 (representing the struts). The pressure amplitudes are respectively 5,000Pa and 250Pa at 4·5mm upstream of the rim seal. The 5th symbol in Fig. 8 presents the sealing effectiveness for a computation with only the NGV perturbation (N = 28). The comparison with the 3rd symbol confirms there is little influence of using N = 28 instead of N = 26 (actual number of NGVs). The computation taking into account the influence of both the NGVs and the struts is represented by the 6th symbol. Ingestion is stronger, in good agreement with the measurements. Even if the amplitude of the larger scale asymmetry may be overestimated, this shows the possible influence of such components. A final test is performed by adding a 1/7th power law velocity boundary layer profile at the annulus inlet. Even assuming a boundary layer thickness of half the annulus height (7th symbol), this is found to have little influence on ingestion.

4.0 REPRESENTATIVE GEOMETRY (RIG C)

This section presents the numerical study of a turbine stage with a cavity located between the stator and rotor discs. The design of the cavity agrees with the industrial guidelines presented in the introduction: the seal is of chute type, with the stator overlapping the rotor, and inner seals separate the cavity into different sections. The vanes,

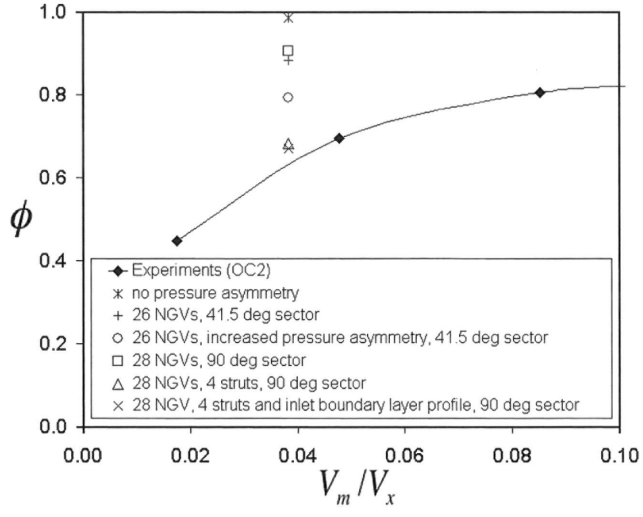

Figure 8. [rig A] Sealing effectiveness at r/r_{hub} = 0·95 and V_m/V_x = 0·038, for a high annulus mass flow (V_x = 100ms^{-1}), with different kind of asymmetries enforced in the computations.

https://doi.org/10.1017/S000192400070042X Published online by Cambridge University Press

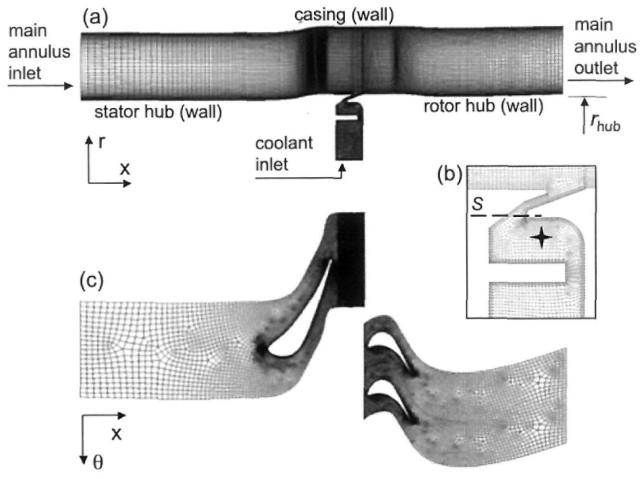

Figure 9. [rig C] a) Lateral view of the grid, b) close up view of the rim seal (dashed line: cutting surface *S* used to calculate ψ, star: spectrum extraction point) and c) upper view (θ = 0deg corresponds to the vane trailing edge). The main annulus height is 0·0252m, and the domain extends over 0·180m in the axial direction. The cavity height is 0·025m (between the bottom and the main annulus hub radius).

the blades and the details of the cavity are all included in the CFD model, making this study particularly representative of an aero-engine. Furthermore, experimental results obtained at the University of Sussex[10, 11] are presented to support the numerical approach. This involves steady pressure and tracer gas measurements (CO_2 seeding in the coolant flow supply).

Unsteady computations are carried out on a domain enclosing the vanes, the upper two sections of the cavity ($r/r_{hub} > 0{\cdot}84$), and the blades, as shown in Fig. 9. A non-linear time marching approach is applied, with a sliding plane at the interface between the stator and the rotor. This latter point requires the same angular extent between the stator and the rotor domains, which is achieved using a ratio of 27:54 for the number of vanes:blades, instead of 26:59 as in the experiment. This allows the reduction of the computational domain to one vane and two blade passages. Figure 9 presents a view of the grid: the total number of points is about $1{\cdot}3 \times 10^6$. Steady computations have also been carried out in the static frame of reference (suppressing the blades) and in the rotating frame of reference (suppressing the vanes), in order to separate the influences of the two rows. The mesh is similar to the unsteady one around the vanes / blades and inside the cavity, corresponding to $0{\cdot}84 \times 10^6$ grid points for the static steady computation (one vane passage) and $0{\cdot}46 \times 10^6$ grid points for the rotating steady computation (one blade passage).

The computations are carried out using HYDRA, a finite volume CFD solver developed by Rolls-Royce and partners. RANS equations are solved using the Spalart-Allmaras turbulence model[16]. Time advancement is implicit, with a CFL (Courant-Friedrichs-Lewy) number of 2·0, and 100 time steps per blade passing period for the unsteady computations. Fluxes are discretised using a centred scheme (2nd order), with a 2nd order smoothing (1st order around the shocks) for the inviscid components. The inlets, in the main annulus (main inlet) and at the bottom of the cavity (coolant inlet), are represented by a subsonic inflow condition where the stagnation temperature, the stagnation pressure and the flow angles are imposed. The outlet is represented by a subsonic outflow condition (static pressure imposed), with a radial equilibrium gradient when the outlet is located in the high swirl region just downstream of the vanes. Also, circumferential periodicity is applied on the sides of the domain. Finally, no-slip conditions with wall functions are imposed on the walls, with $y^+ \in [15;80]$. Steady convergence is assessed by the stagnation of the residuals after a decreasing by a factor of 10^{-6} or less, and unsteady convergence by reaching a periodic state (±3% on pressure probes). The mass flow error is lower than 1%. The unsteady computations are run for 700 blade-passing periods because of the slower convergence at the bottom of the cavity than in the main passage. On the same number of processors (eight recent CPUs), computational time is about three days for the steady computation on 0·46 million grid points (rotating frame), and seven weeks for the unsteady computations (despite the modified vanes:blades ratio of 1:2).

Table 1 presents the experiments and the computations. The names are constructed in the following way: the operating condition (Design/OffDesign) and the level of coolant flow (1: low, 2: medium), the kind of result (Steady/Unsteady/Experiment) and finally the frame of reference for the steady computations (str: stator, rtr: rotor). First, three experiments are presented. The comparison between OffDesign1-Experiment and Design1-Experiment shows the influence of the operating condition, for a similar coolant flow level (V_m/V_x). Then, comparing Design1-Experiment and Design2-Experiment shows the influence of the coolant flow level, at a given operating condition. Five computations are then presented. Three unsteady computations are carried out at similar conditions to the three experiments: OffDesign1-Unsteady, Design1-Unsteady and Design2-Unsteady. Finally, a steady computation is presented in each frame of reference (stator and rotor), at the condition Design1: Design1-Steady-str and Design1-Steady-rtr. These two computations allow the influence of each row to be separated.

Figure 10 presents the time-averaged pressure coefficient on the hub, 1·5mm downstream of the vane trailing edges, as a function of the circumferential angle:

$$C_p = \frac{P - P_{mean}}{P_{0i} - P_{mean}} \quad \ldots(8)$$

where P_{mean} is the mean pressure over the circumference and P_{0i} the stagnation pressure upstream of the vanes. Computation Design1-Steady-rtr is not represented because it does not take into account the

Table 1
[rig C] Experimental and computational conditions. ϕ is calculated using Equation (4) and the measured tracer gas concentration (at r/r_{hub} = 0·96 and θ = 0deg on the stator disc). ψ is a global quantity, comparable to ϕ (cf. Appendix).

	main inlet mas flow (kg/s)	Re_x	Re_θ	C_w	V_m/V_x
OffDesign1-Experiment	1·350	3·85e+5	6·63e5	1,512	0·0838 ϕ = 0·76
Design1-Experiment	4·578	1·31e+6	1·98e+6	5,570	0·0913 ϕ = 0·60
Design2-Experiment	4·574	1·31e+6	2·06e+6	7,537	0·1170 ϕ = 0·75
OffDesign1-Unsteady	1·285	3·54e+5	5·63e+5	1,251	0·0808 ψ = 0·96
Design1-Unsteady	4·470	1·13e+6	1·78e+6	4,553	0·0746 ψ = 0·72
Design2-Unsteady	4·453	1·12e+6	2·00e+6	7,787	0·1250 ψ = 0·99
Design1-Steady-str	4·480	1·13e+6	1·78e+6	4,612	0·0758 ψ = 1·00
Design1-Steady-str	4·546	1·15e+6	1·84e+6	4,293	0·0699 ψ = 0·93

https://doi.org/10.1017/S000192400070042X Published online by Cambridge University Press

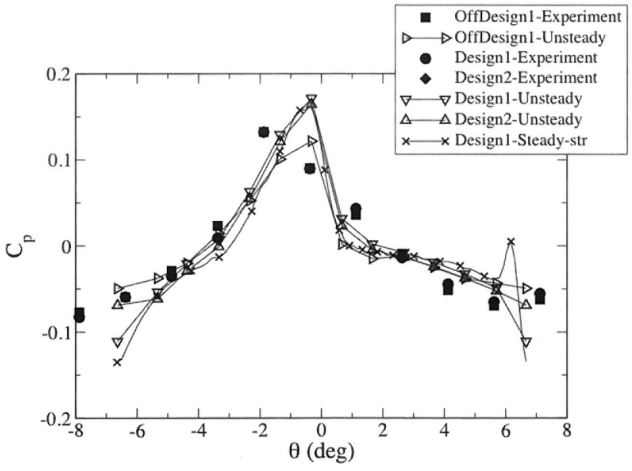

Figure 10. [rig C] Average pressure coefficient on the annulus hub, 1·5mm downstream of the vane trailing edge.

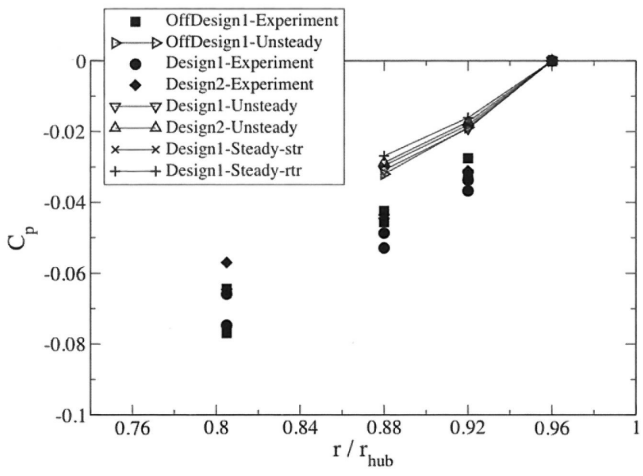

Figure 11. [rig C] Average pressure coefficient inside the cavity, on the stator face at θ = 0deg .

wakes of the vanes. The agreement between experiments and computations is reasonable, with merging of the curves due to the non-dimensionalisation. The pressure asymmetry generated by the vanes in the annulus represents about 25%-30% of the dynamic head ($P_{0i} - P_{mean}$).

Figure 11 presents the time-averaged pressure coefficient on the stator face of the cavity, at the angular position corresponding to the vane trailing edge (θ = 0 deg):

$$C_p = \frac{P - P_{(r/r_{hub}=0{\cdot}96)}}{0{\cdot}5\rho_{(r/r_{hub}=0.96)}(r_{hub}\Omega)^2} \quad \ldots (9)$$

where $P_{(r/r_{hub}=0{\cdot}96)}$ and $\rho_{(r/r_{hub}=0{\cdot}96)}$ are the mean pressure and density at $r/r_{hub} = 0{\cdot}96$. Again, owing to the non-dimensionalisation, the curves merge for both the experiments and the computations. However, the pressure gradient is smaller in the computations. This could be due to an underestimate of the entrainment by the rotor disc. It could also result from an underestimated ingestion inside the cavity, because the main annulus flow is highly swirling and so increases the radial pressure gradient.

In the experiment, ingestion inside the cavity is assessed by the sealing effectiveness ϕ, which is calculated using Equation (4) and the tracer gas concentration at $r/r_{hub} = 0{\cdot}96$ and θ = 0deg (vane trailing-edge angle) on the stator disc. The results are given in Table 1. The strongest ingestion is obtained at the design operating condition, for the lowest coolant flow rate (Design1-Experiment: ϕ = 0·60). As expected, ingestion is reduced when increasing the coolant flow rate (Design2-Experiment: ϕ = 0·75). More surprisingly, ingestion is also reduced when moving to off-design operating condition (OffDesign1-Experiment: ϕ = 0·76). For the computations, a passive scalar option would be necessary to represent the tracer gas and to calculate ϕ. As this option is not currently available, another quantity is used to estimate ingestion: the mass flow ratio through the rim seal (ψ), as explained in appendix.

$$\psi = 1 - \overline{m_{in}} \Big/ \overline{m_{out}} \quad \ldots (10)$$

where $\overline{m_{in}}$ and $\overline{m_{out}}$ are the time-averaged inward and outward mass flows measured through the rim seal (cutting surface S presented in Fig. 9). The computed values of ψ are presented in Table 1.

Considering the three unsteady computations, the values of ψ are high, but respect the experimental trends obtained on ϕ. Indeed, as explained in the appendix, only a qualitative comparison should be made between ϕ and ψ. Ingestion is higher at design condition with the lower coolant flow rate (Design1-Unsteady: ψ = 0·72). Ingestion is reduced either by increasing the coolant flow rate (Design2-Unsteady: ψ = 0·99) or by moving to off-design condition (OffDesign1-Unsteady: ψ = 0·96). This prediction of the experimental trends is encouraging, particularly the decrease in ingestion at the off-design condition. However, the high values of ψ and the underestimate of the pressure gradient previously noticed inside the cavity, appear as signs of a global underestimate of ingestion. This could result from limitations of the computational procedure, or from the influence of large-scale asymmetries in the experiment (struts…), as discussed in Section 3. Finally, concerning the two steady computations, only the one in the rotating frame (Design1-Steady-rtr: ψ = 0·93) shows ingestion. This indicates the higher influence of the rotor blades on ingestion, for this configuration. However, the value obtained by this steady computation remains much higher than for the unsteady computation (Design1-Unsteady: ψ = 0·72), which shows the importance of unsteady effects.

The first three plots in Fig. 12 present the radial velocity spectra calculated in the upper section of the cavity at the point shown in Fig. 9 for the three unsteady computations. At both operating conditions, the peak corresponding to the blade passing frequency appears, but its level is higher at the design condition, probably due to the higher potential effect of the blades. More interestingly, at design condition and for the lower coolant flow rate (Design1-Unsteady), other components appear at lower frequencies. They are dominated by $f/f_{bld} = 0{\cdot}44$, which could be due to an instability such as those observed in Section 2.

In this paragraph, a digression is made to consider a computation similar to Design1-Unsteady, but without any vanes or blades. This allows isolation of the unsteady effects due to the cavity, from the effects due to the vanes and the blades. Moreover, this computation is done on a wider circumferential sector (120deg) to lower the influence of the periodic boundary conditions. In Figs 12 and 13, this modified version of Design1-Unsteady is clearly labelled by the comment: 'Isolated cavity, 120deg sector'. Looking at the Fourier transform in Fig. 12 (last spectrum), a peak appears with an amplitude of 0·51ms^{-1}, spreading around $f/f_{bld} = 0{\cdot}31$. Considering the axisymmetric geometry and boundary conditions of this computation, this must be due to an instability. Figure 13 presents the radial velocity in a cross-section through the cavity and the main annulus ($x = x_{stator} + 0{\cdot}7(x_{rotor} - x_{stator})$), where a circumferential pattern is

https://doi.org/10.1017/S000192400070042X Published online by Cambridge University Press

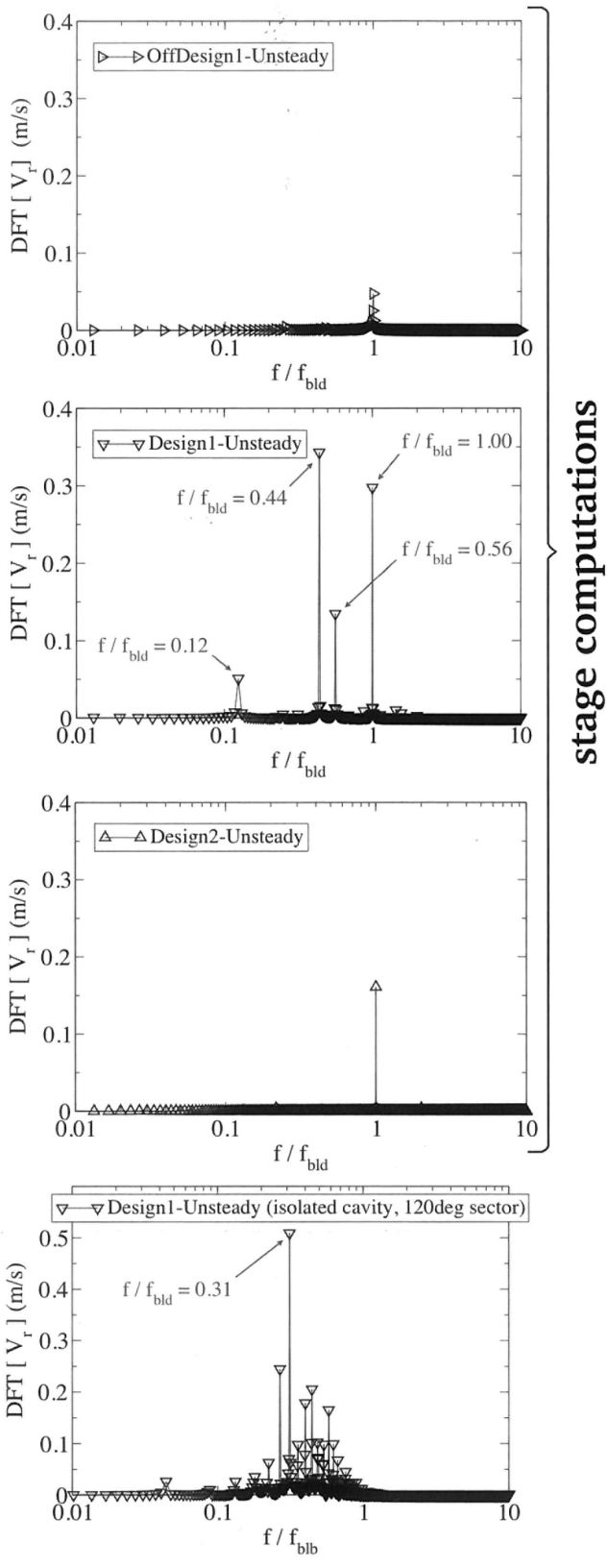

Figure 12. [rig C] Discrete Fourier Transform of the radial velocity at the point location presented in Fig. 9: ($x = x_{stator} + 0{\cdot}6\ (x_{rotor} - x_{stator})$, $r/r_{hub} = 0{\cdot}96$, $\theta = -3{\cdot}1$ deg).

observed in the region of the rim seal. The study of the correlation of circumferentially distributed pressure probes then shows that this pattern is made of 21 dominant lobes over 360deg, rotating at $0{\cdot}80\Omega$, which is consistent with the dominant component $f/f_{bld} = 0{\cdot}31$. The wide circumferential sector also allows other wavelengths corresponding to fractions of the sector to develop, generating the neighbouring frequencies around $f/f_{bld} = 0{\cdot}31$. As the dominant fluctuations are located within the rim seal, a possible source of instability could be the inflexion points in the velocity profiles generated inside the rim seal by the inward and outward flows.

Focusing again on the stage computations, the component $f/f_{bld} = 0{\cdot}44$ in Design1-Unsteady can be explained by the instability observed in the previous paragraph in the isolated cavity (around $f/f_{bld} = 0{\cdot}31$). The corresponding amplitudes are similar between the two computations in Fig. 12. However, the smaller circumferential sector of the stage computation imposes a number of lobes proportional to 27 over the circumference, resulting in a higher frequency of the instability ($f/f_{bld} = 0{\cdot}44$ instead of $f/f_{bld} = 0{\cdot}31$) and the suppression of the neighbouring frequencies. The other frequencies appearing in the stage computation Design1-Unsteady (cf. Fig. 12) must come from non-linear interactions between the instability frequency ($f/f_{bld} = 0{\cdot}44$) and the blade passing frequency ($f/f_{bld} = 1{\cdot}00$). They can be obtained by the following combinations: $0{\cdot}56 = 1{\cdot}00 - 0{\cdot}44$ and $0{\cdot}12 = 0{\cdot}56 - 0{\cdot}44$. Such non-linear effects might be expected to develop when the amplitude of the perturbation from the blades inside the rim seal is similar to the amplitude of the instability, as in this case. This can generate low frequency fluctuations (here: $f/f_{bld} = 0{\cdot}12$), which are more effective in driving the flow through the seal, taking into account the relatively small radial velocities inside the rim seal. Also, frequencies close to an acoustic resonance of the cavity may be generated this way, which may also increase ingestion.

As a final illustration, Fig. 14 shows the instantaneous radial velocity on a constant radius surface just above the main annulus hub ($r = r_{hub} + 0{\cdot}5$mm), for the unstable stage computation: Design1-Unsteady. This shows the influence of the vane wakes and blade potential effects near the rim seal. However, according to the results of the steady computations, ingestion is more influenced by the blades. But, it is also possible to see in Fig. 14 that the flow through the rim seal is dominated by the same circumferential periodicity as the vanes. Actually, this pattern is rotating and corresponds to the instability inside the rim seal, whose wavelength is enforced to match the domain angular sector (equal to the vane pitch).

Finally, the computational results explain the strong ingestion obtained at design condition (Design1), compared to the corresponding

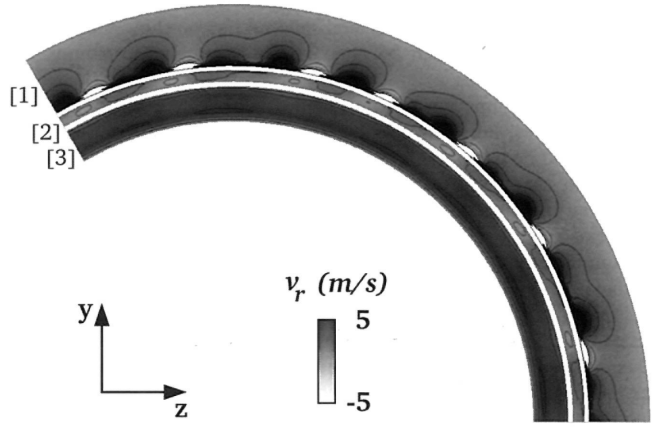

Figure 13. [rig C] Instantaneous radial velocity on an x-plane at 70% across the cavity ($x = x_{stator} + 0{\cdot}7(x_{rotor} - x_{stator})$), for computation Design1-Unsteady (isolated cavity, 120 deg sector). [1]: main annulus, [2]: upper section of the cavity, [3]: lower section of the cavity.

https://doi.org/10.1017/S000192400070042X Published online by Cambridge University Press

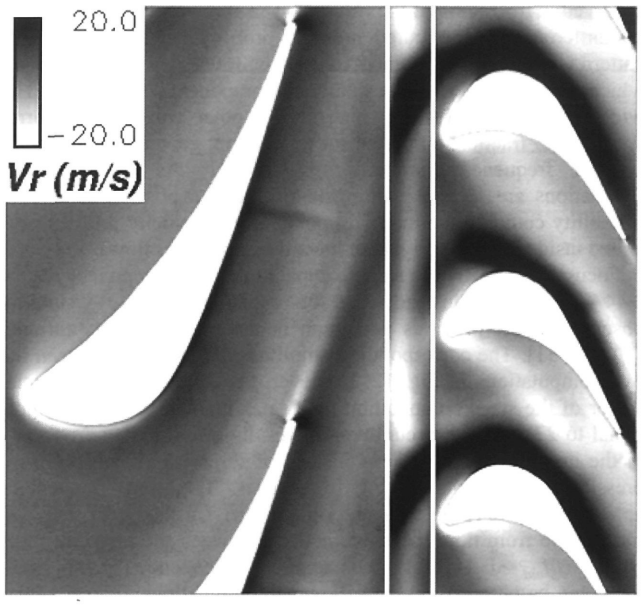

Figure 14. [rig C] Instantaneous radial velocity at $r = r_{hub}$ + 0·5mm, for computation Design1-Unsteady. The vanes are on the left hand side (upstream), the blades on the right hand side (downstream), and the rim seal outlet is delimited by the two vertical white lines.

off-design condition (OffDesign1). The design condition is characterized by a higher potential effect of the blades (which increases with Re_x), but also by the instability generated inside the rim seal by the pumping effect (which increases with Re_θ). Also, the higher Mach number expected at design condition could promote the non-linear effects.

5.0 CONCLUSIONS

Results of CFD studies into turbine rim seal ingestion have been presented and compared to experimental data. It has been found that for a simple axial seal with weak external flow, the ingestion driven by disc pumping involves an unsteady three-dimensional flow. For this seal the unsteadiness is suppressed by the external flow, as would be encountered for the outer seal in an engine. However, further CFD results, confirmed by experimental measurements, show that similar unsteady phenomena can be encountered at engine conditions for other seal geometries.

Pressure asymmetries in the annulus, due to the stationary and moving blades, are shown to have a major influence on ingestion. Care should be taken in experimental studies or engine design calculations to account for any large-scale circumferential asymmetries due to struts or other inlet distortions. These may be relatively slow to decay axially and can have a significant effect on ingestion even though the amplitude of these asymmetries might be small compared to that due to the adjacent blades and vanes.

Finally, the application of CFD to a realistic turbine stage illustrates the state-of-the-art for coupled disc cavity/main annulus flows. Despite the long computational time required, the non-linear time marching computations are the most able to capture the effects of modifying the operating condition or the coolant mass flow. Moreover, in this case, a deeper analysis of the computations shows the strong influences of the potential effect of the rotor blades and of a flow instability developing inside the rim seal. Also, the appearance of non-linear coupling frequencies is noted, and this effect has to be considered carefully in future studies.

ACKNOWLEDGEMENTS

The authors wish to acknowledge the DTI and the EPSRC for their support within the PUMA DARP project, together with Rolls-Royce plc and Alstom for their support for these research activities.

REFERENCES

1. VON KARMAN, T. Uber laminare und turbulente Reibung, *Zeitschrift für angewandte Mathematik und Mechanik*, 1921, **1**, pp 233-252.
2. BATCHELOR, G.K. Note on a class of solutions of the Navier-Stokes equations representing steady rotationally-symmetric flow, *Quart J Mech and Applied Math,* 1951, **4,** pp 29-41.
3. SERRE, E., BONTOUX, P. and LAUNDER, B.E. Direct numerical simulation of transitional turbulent flow in a closed rotor-stator cavity, *Flow Turbulence and Combustion*, 2002, **69,** pp 35-50.
4. OWEN, J.M. and ROGERS, R.H. *Flow and heat transfer in rotating-disc systems,* Volume 1 — rotor-stator systems, Research Studies Press, Taunton, Somerset (UK), 1989.
5. PHADKE, U.P. and OWEN, J.M. Aerodynamics aspects of the sealing of gas turbine rotor-stator systems Part II: the performance of simple seals in a quasi-axisymmetric external flow, *Int J Heat and Fluid Flow*, 1988, **9,** (2), pp 106-112.
6. PHADKE, U.P. and OWEN, J.M. Aerodynamic aspects of the sealing of gas turbine rotor-stator systems Part I: the behaviour of simple shrouded rotating-disc systems in a quiescent environment, *Int J Heat and Fluid Flow,* 1988, **9,** (2), pp 98-105.
7. BAYLEY, F.J. and OWEN, J.M. The fluid dynamics of a shrouded disc system with a radial outflow of coolant, *ASME J Engineering for Power,* 1970, **92,** pp 335-341.
8. CHEW, J.W. A theoretical study of ingress for shrouded rotating disc systems with radial outflow, Transactions of the ASME, *J of Turbomachinery,* 1989, **113,** pp 91-97.
9. SCANLON, T., WILKES, J., BOHN, D. and GENTILHOMME, O. A simple method for estimating ingestion of annulus gas into a turbine rotor stator cavity in the presence of external pressure variations, Proceedings of ASME Turbo Expo 2004, GT2004-53097, 14-17 June 2004, Vienna (Austria).
10. GENTILHOMME, O., HILLS, N.J., TURNER, A.B. and CHEW, J.W. Measurement and analysis of ingestion through a turbine rim seal, Proceedings of ASME Turbo Expo 2002, GT-2002-30481, June 3-6, 2002, Amsterdam.
11. GENTILHOMME, O. Turbine Rim Seal Ingestion, PhD Thesis, University of Sussex, 2004.
12. FLUENT, http://www.fluent.com.
13. WOLFSTEIN, M. The velocity and temperature distribution of one-dimensional flow with turbulence augmentation and pressure gradient, *Int J Heat and Mass Transfer,* 1969, **12,** pp 301-318.
14. CAO, C., CHEW, J.W., MILLINGTON, P.R., and HOGG, S.I. Interaction of rim seal and annulus flows in an axial flow turbine, Proceedings of the ASME Turbo Expo 2003, GT2003-38368, June 16-19, 2003, Atlanta (USA), also to appear in *ASME J Eng for Gas Turbines and Power.*
15. CHEW, J.W., GREEN, T. and TURNER, A.B. Rim sealing of rotor stator wheelspaces in the presence of external flow, ASME Paper 94-GT-126, 1994.
16. SPALART, P.R., ALLMARAS, S.R. A one-equation turbulence model for aerodynamic flows, *La Recherche Aerospatiale,* 1994, **1,** pp 5-21.

APPENDIX

This appendix describes the construction of the mass flow ratio through the rim seal(ψ), which is used to estimate ingestion in the computations when the passive scalar option is not available.

A simplified representation of the upper section of the cavity (e.g. rig C) is presented in Fig. 15, and two hypotheses are made:
(*i*) There is no major ingestion in the lower section of the cavity. This is a reasonable hypothesis, the upper section damping the pressure asymmetries from the annulus (cf. Introduction).
(*ii*) The flow ingested inside the cavity, through the rim seal, comes from the main annulus inlet, and does not contain coolant flow being re-ingested.

https://doi.org/10.1017/S000192400070042X Published online by Cambridge University Press

In these conditions, the mass flow entering the cavity at the bottom is m_{cool}, and the inward and outward mass flows through the rim seal are defined by:

$$m_{in} = 1/2 \int_S \rho.(|\mathbf{v}.\mathbf{n}| - \mathbf{v}.\mathbf{n}).\mathrm{d}S \quad ; \quad m_{out} = 1/2 \int_S \rho.(|\mathbf{v}.\mathbf{n}| + \mathbf{v}.\mathbf{n}).\mathrm{d}S \qquad \ldots (11)$$

where S is a cutting surface through the rim seal, and $\mathbf{n}$ the local unity vector normal to the surface (outward direction).

Taking into account that m_{cool} is composed only of flow coming from the coolant inlet, and m_{in} only of flow coming from the main annulus inlet, the average concentration of coolant flow in the upper section of the cavity can be estimated by:

$$\psi = \frac{\int_0^T m_{cool}\,\mathrm{d}t}{\int_0^T (m_{cool} + m_{in})\,\mathrm{d}t} = \frac{\overline{m_{cool}}}{\overline{m_{cool}} + \overline{m_{in}}}$$

($t \in [0;T]$ being a representative period of time)

Then, the mass conservation gives: $\overline{m_{out}} = \overline{m_{in}} + \overline{m_{cool}}$

so: $$\psi = \frac{\left(\overline{m_{out}} - \overline{m_{in}}\right)}{\left(\overline{m_{out}} - \overline{m_{in}}\right) + \overline{m_{in}}} = 1 - \overline{m_{in}} \Big/ \overline{m_{out}}$$

ψ is an estimate of ϕ, but there are limitations coming from the hypotheses. The re-ingestion of coolant flow through the rim seal is not taken into account, which tends to lower ψ compared to ϕ (particularly for long rim seal ducts with fluctuating flow direction inside). Conversely, only ingestion by convection is considered, not by diffusion, and this tends to increase ψ. Consequently, ψ can be used to estimate ingestion in the computations, for qualitative but not quantitative comparison with ϕ.

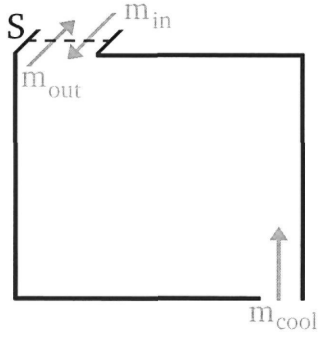

Figure 15. Sketch of the upper section of the cavity, presenting the mass flows and the cutting surface S through the rim seal.

https://doi.org/10.1017/S000192400070042X Published online by Cambridge University Press